nanomaterials

MDPI

Article

Enhanced High-Temperature (600 °C) NO_2 Response of $ZnFe_2O_4$ Nanoparticle-Based Exhaust Gas Sensors

Adeel Afzal [1,*], Adnan Mujahid [2], Naseer Iqbal [1], Rahat Javaid [3] and Umair Yaqub Qazi [1,4]

1 Department of Chemistry, College of Science, University of Hafr Al Batin, P.O. Box 1803, Hafr Al Batin 39524, Saudi Arabia; naseeriqbal@uhb.edu.sa (N.I.); umair_qazi@yahoo.com (U.Y.Q.)
2 Institute of Chemistry, University of Punjab, Quaid-i-Azam Campus, Lahore 54590, Pakistan; adnan.mujahid@pu.edu.pk
3 Renewable Energy Research Center, Fukushima Renewable Energy Institute, National Institute of Advanced Industrial Science and Technology, AIST, 2-2-9 Machiikedai, Koriyama, Fukushima 963-0298, Japan; rahat.javaid@aist.go.jp
4 Division of Nanomaterials and Chemistry, Hefei National Laboratory for Physical Sciences at Microscale, University of Science and Technology of China, Hefei 230026, China
* Correspondence: aa@aafzal.com; Tel.: +966-13-720-3426 (ext. 1675)

Received: 7 September 2020; Accepted: 21 October 2020; Published: 27 October 2020

Abstract: Fabrication of gas sensors to monitor toxic exhaust gases at high working temperatures is a challenging task due to the low sensitivity and narrow long-term stability of the devices under harsh conditions. Herein, the fabrication of a chemiresistor-type gas sensor is reported for the detection of NO_2 gas at 600 °C. The sensing element consists of $ZnFe_2O_4$ nanoparticles prepared via a high-energy ball milling and annealed at different temperatures (600–1000 °C). The effects of annealing temperature on the crystal structure, morphology, and gas sensing properties of $ZnFe_2O_4$ nanoparticles are studied. A mixed spinel structure of $ZnFe_2O_4$ nanoparticles with a lattice parameter of 8.445 Å is revealed by X-ray diffraction analysis. The crystallite size and X-ray density of $ZnFe_2O_4$ nanoparticles increase with the annealing temperature, whereas the lattice parameter and volume are considerably reduced indicating lattice distortion and defects such as oxygen vacancies. $ZnFe_2O_4$ nanoparticles annealed at 1000 °C exhibit the highest sensitivity (0.13% ppm^{-1}), sharp response (τ_{res} = 195 s), recovery (τ_{rec} = 17 s), and linear response to 100–400 ppm NO_2 gas. The annealing temperature and oxygen vacancies play a major role in determining the sensitivity of devices. The plausible sensing mechanism is discussed. $ZnFe_2O_4$ nanoparticles show great potential for high-temperature exhaust gas sensing applications.

Keywords: annealing temperature; chemiresistors; gas sensors; oxygen vacancies; sensing mechanism; $ZnFe_2O_4$ nanoparticles

1. Introduction

Hazardous exhaust gases such as nitrogen dioxide (NO_2) and sulfur dioxide (SO_2) are the major atmospheric pollutants [1]. The European Union's (E.U.) ambient air quality directives have set the hourly NO_2 concentration threshold as 200 $\mu g/m^3$ [2]. According to the European Environment Agency (EEA) report published in 2016, NO_2 pollution was responsible for 71,000 premature deaths in the E.U. [3]. Thus, it is important to detect the emission and subsistence of NO_2 in indoor and outdoor air. The main source of NO_2 pollution is the exhaust emissions as a result of the combustion processes in motor vehicles and manufacturing industries [4]. The direct inspection of the exhaust emissions requires devices that can detect NO_2 at high temperatures, i.e., usually ≥500 °C [5]. In this regard,

metal oxide-based electronic gas sensors are the most sought-after devices for applications in harsh environments [6–8].

According to a recent review of high-temperature gas sensors, Ghosh et al. [9] noted the majority of the metal oxide-based gas sensors work at moderately high temperatures only, while the sensitivity of metal oxides is substantially influenced at temperatures above 350 °C. Albeit a large number of metal oxide-based NO_2 gas sensors are reported [10–13], only a few work at high temperatures, i.e., ≥600 °C. For instance, Miura et al. [14] reported Yt-stabilized zirconia and spinel $ZnFe_2O_4$ sensing electrodes for the electrochemical detection of NO_x at 600–700 °C. However, chemiresistive-type NO_2 gas sensors for high-temperature applications are rarely reported [13,15,16]. Therefore, the fabrication of high-temperature NO_2 gas sensors for harsh environments is highly desired due to their widespread applications in all types of combustion systems.

This article reports the first high-temperature thick film chemiresistive gas sensor for NO_2 detection at 600 °C. The sensor is based on highly stable spinel zinc ferrite ($ZnFe_2O_4$) nanoparticles prepared via a solid-state, high-energy ball-milling (HEBM) process followed by high-temperature thermal annealing at different temperatures (600, 800, and 1000 °C). $ZnFe_2O_4$ nanoparticles have been used for the detection of toxic organic vapors and gases such as acetone at 260 [17] and 275 °C [18], ethanol at 27 [19] and 220 °C [20], toluene at 300 °C [21], H_2S at 85 °C [22] and 135 °C [23], and O_2 at 180 °C [24]. Recently, Runa et al. [25] fabricated a chemiresistive NO_2 gas sensor using ZnO/$ZnFe_2O_4$ composites with p-n heterostructure, which revealed excellent selectivity and high gas response toward 0.1–20 ppm NO_2 compared to pure ZnO. However, the gas response diminished rapidly at temperatures of ≥220 °C [25]. In this work, the effects of high-temperature annealing on the crystal structure and NO_2 gas sensing properties are studied. The cubic spinel $ZnFe_2O_4$ nanoparticles are stable at high temperatures and demonstrate excellent NO_2 sensing capability at 600 °C with fast response and recovery times.

2. Materials and Methods

Iron(III) oxide (Fe_2O_3 nanopowder) and zinc oxide (ZnO nanopowder) obtained from MilliporeSigma (Merck KGaA, Darmstadt, Germany) were used to prepare $ZnFe_2O_4$ nanoparticles. $ZnFe_2O_4$ nanoparticles were synthesized by high-energy ball milling (HEBM) process using a SPEX™ 8000M Mixer/Mill™ (SPEX® SamplePrep, New Jersey, NJ, USA). The ball mill was equipped with a 500-cc stainless steel vessel containing stainless steel balls for mechanical milling of Fe_2O_3 and ZnO. The mass ratio of steel balls and chemical powders was fixed at 50:1. HEBM was performed under ambient conditions for 2 h at 600 rpm. The product was subsequently vacuum annealed at 600, 800, and 1000 °C for 2 h, and characterized. Corresponding to the annealing temperature (600–1000 °C), the samples were abbreviated as $ZnFe_2O_4$-600, $ZnFe_2O_4$-800, and $ZnFe_2O_4$-1000, respectively.

The crystal structure of the annealed $ZnFe_2O_4$ nanoparticles was studied with a STOE STADI P X-ray diffractometer (XRD) (STOE & Cie GmbH, Darmstadt, Germany) using a Cu Kα irradiation source (λ = 1.5406 Å). The samples were scanned in the 2θ range of 10°–90° with a scan rate of 2°/min. The crystallite size (D) is determined by the Scherrer's formula [26] ($D = K\lambda/B\cos\theta$), where K is a numerical factor referred to as the crystallite-shape factor with an approximate value of 0.89, λ is the wavelength of the X-rays, B is full-width at half-maximum of the most intense (311) diffraction peak in radians, and θ is the Bragg angle. The experimental lattice parameter (a), X-ray density (ρ_{xrd}), and the specific surface area (S_A) are also calculated from the XRD data of annealed $ZnFe_2O_4$ nanoparticles, as described elsewhere [27,28].

The microstructure and surface morphology of $ZnFe_2O_4$ nanoparticles were studied with a JEOL JSM-6510 scanning electron microscope (SEM) (JEOL Ltd., Tokyo, Japan). The elemental composition of $ZnFe_2O_4$ nanoparticles was determined with the energy-dispersive X-ray spectroscopy (EDS) (JEOL Ltd., Tokyo, Japan).

Thick-film chemiresistor-type gas sensors were fabricated by mixing an appropriate amount of $ZnFe_2O_4$-600, $ZnFe_2O_4$-800, and $ZnFe_2O_4$-1000 nanoparticles with absolute ethanol to make a thick

slurry, which was subsequently drop-coated onto alumina micro-hotplates with vapor-deposited platinum (Pt) contacts. The devices were placed in a vacuum oven at 80 °C for 2 h to dry and stabilize the sensing element. The chemiresistor-type devices were installed in a gas sensing chamber fitted with the electrical connections and the gas inlet and outlet. The measurements were performed with a Keithley 6517A electrometer. The sensor responses were measured simultaneously at 600 °C for 100–400 ppm of NO_2 gas. The sensor response (S) is defined as $S(\%) = (R_g - R_a) \times 100/R_a$, where R_a and R_g are the resistances in air and (100–400 ppm) NO_2 gas.

3. Results and Discussion

Figure 1 shows the XRD pattern of as-synthesized ball-milled $ZnFe_2O_4$ nanoparticles, referred to as BM-$ZnFe_2O_4$. The HEBM process yields crystalline BM-$ZnFe_2O_4$ nanoparticles with a cubic spinel lattice structure as indicated by the presence of characteristic (311) diffraction at 35.22° (2θ) position. The crystallite size (D) of as-synthesized BM-$ZnFe_2O_4$ nanoparticles is 9.30 nm. The lattice parameter (a) is calculated to be 8.445 Å, which is in agreement with the values reported for spinel $ZnFe_2O_4$ nanostructures in the literature and the standard value of bulk $ZnFe_2O_4$ (a = 8.441 Å) [29–31]. The lattice parameter of as-synthesized BM-$ZnFe_2O_4$ nanoparticles is slightly higher (~0.05%) than the standard value that may be inherent to the ball-milling process because an increase in the lattice parameter of ball-milled $ZnFe_2O_4$ samples has been reported earlier [32–34].

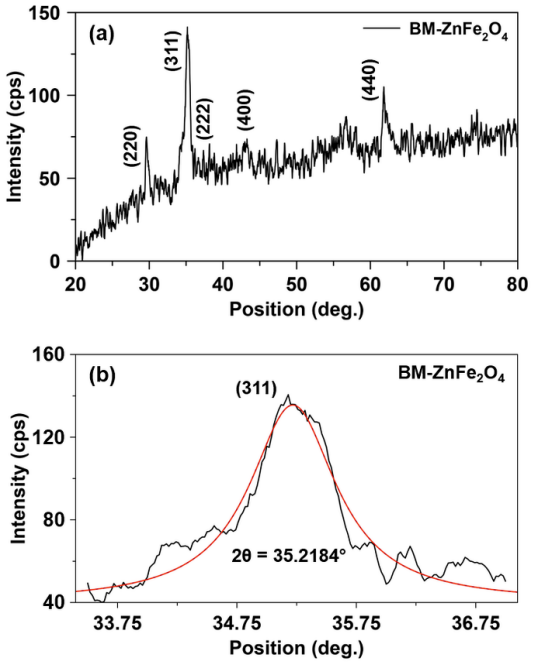

Figure 1. (**a**) X-ray diffraction pattern of the as-synthesized, ball-milled zinc ferrite (BM-$ZnFe_2O_4$) nanoparticles. (**b**) The characteristic (311) plane diffraction of cubic spinel BM-$ZnFe_2O_4$ nanoparticles.

Theoretically, the cation distribution in a perfect normal spinel $ZnFe_2O_4$ unit cell is $(Zn^{2+})_{tet}[Fe^{3+}]_{oct}O_4$, i.e., the tetrahedral (A) and octahedral (B) sites are solely occupied by Zn^{2+} and Fe^{3+} cations, respectively [35]. However, in nanocrystalline $ZnFe_2O_4$ the contrary distributions of Zn^{2+} and Fe^{3+} cations on both A and B sites are observed [36,37], which form mixed (or random) spinel structure. According to Chinnasamy et al. [32], the slight increase in the lattice parameter is attributed to the lattice expansion caused by the occupation of B sites by Zn^{2+} ions. Thus, the XRD pattern of as-synthesized BM-$ZnFe_2O_4$ nanoparticles indicates the formation of a mixed cubic spinel lattice. Nonetheless, BM-$ZnFe_2O_4$ nanoparticles are annealed at different temperatures to examine the effect of annealing on the crystal structure evolution, lattice parameter, crystallite size, and morphology of $ZnFe_2O_4$ nanoparticles.

High-temperature annealing is an important step in the fabrication of $ZnFe_2O_4$ nanoparticles, as it renders stability and improves the physical properties of $ZnFe_2O_4$ [38,39]. Figure 2 shows the XRD patterns of $ZnFe_2O_4$ nanoparticles annealed at 600, 800, and 1000 °C for 2 h. XRD patterns are refined using Match! (version 3.11.1.183) and FullProf programs for phase identification from X-ray powder diffraction. All samples exhibit a crystalline structure with the characteristic diffractions corresponding to the following miller indices: (111), (220), (311), (222), (400), (422), (511), (440), (620), and (533), which conform to the crystallography open database card number 230–0615 [40]. XRD results substantiate the formation of the cubic spinel ferrite structure with the *Fd-3m* space group. Also, the XRD patterns align well with the reported literature for $ZnFe_2O_4$ nanoparticles [30,41,42]. The absence of additional diffraction peaks corresponding to the impurities or unreacted oxides also reveals the formation of a single-phase cubic spinel lattice [40].

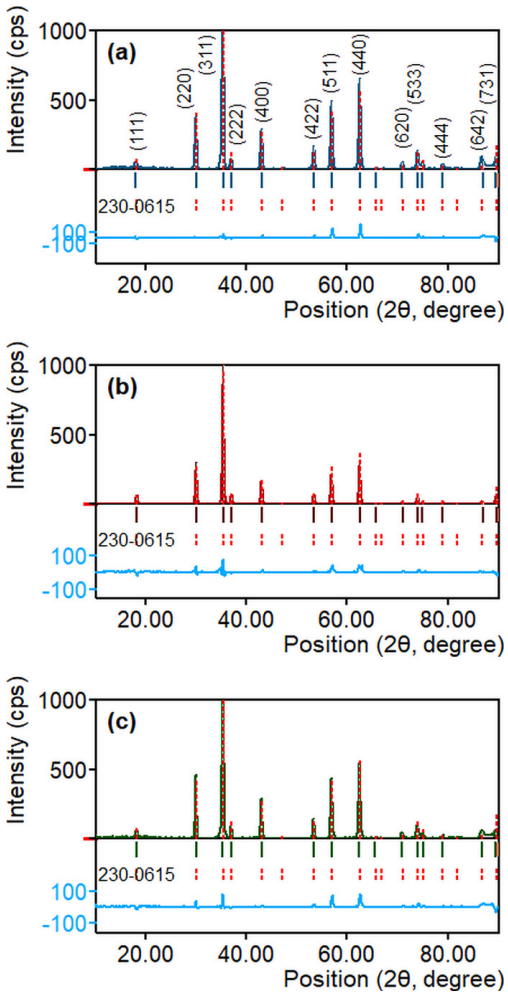

Figure 2. X-ray diffraction patterns of $ZnFe_2O_4$ nanoparticles annealed at different temperatures: (**a**) 600, (**b**) 800, and (**c**) 1000 °C.

Figure 3a–c shows the most intense diffractions of the characteristic (311) plane in $ZnFe_2O_4$ nanoparticles annealed at different temperatures. The XRD data were used to calculate the crystallite size (D), lattice parameter (a), interplanar distance (d_{311}), volume (V), X-ray density (ρ_{xrd}), and specific surface area (S) of the annealed $ZnFe_2O_4$ nanoparticles. Table 1 presents these structural parameters for different samples. The effect of annealing is obvious because of the changes in position and breadth of (311) diffraction peak as a function of the annealing temperature, which reveal variations in the crystallite size and lattice parameter. The position of (311) shifts to a higher 2θ value as the annealing temperature increases.

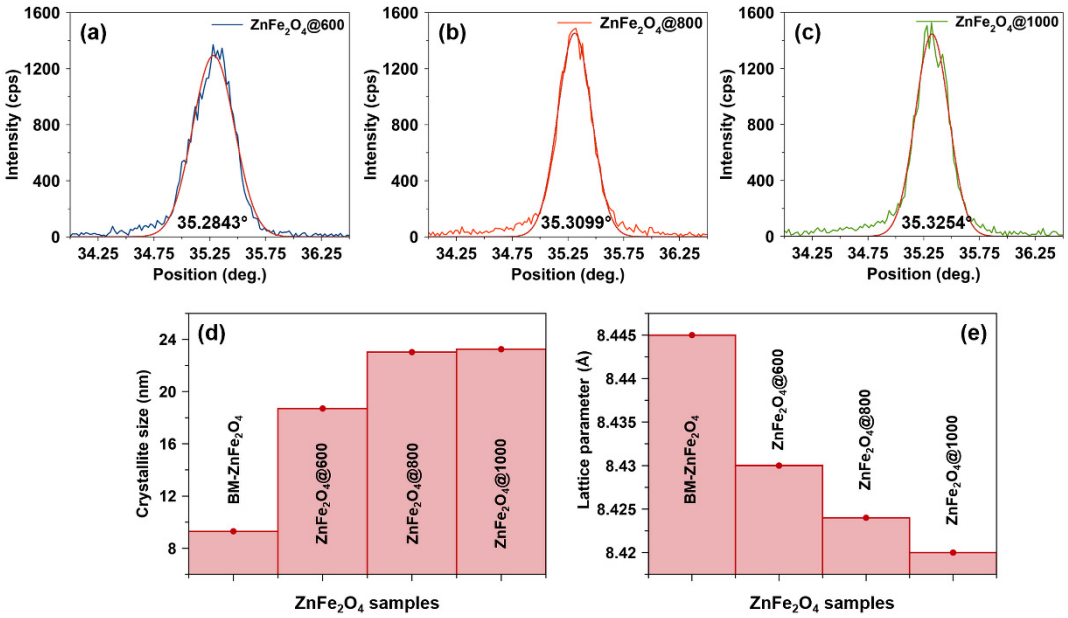

Figure 3. The characteristic (311) plane diffractions of cubic spinel $ZnFe_2O_4$ nanoparticles annealed at (**a**) 600, (**b**) 800, and (**c**) 1000 °C. (**d**) The crystallite size, and (**e**) lattice parameter of $ZnFe_2O_4$ nanoparticles as a function of annealing temperature.

As shown in Figure 3d, the crystallite size of $ZnFe_2O_4$ nanoparticles increases with the annealing time, which is certainly comprehensible because annealing results in grain growth, and the higher the temperature, the greater is the crystallite size [43–45]. The annealing at 600 °C doubles the crystallite size of $ZnFe_2O_4$@600 nanoparticles compared to as-synthesized BM-$ZnFe_2O_4$ nanoparticles. While annealing at 800 °C results in a further increase in the crystallite size, the crystallite sizes of $ZnFe_2O_4$@800 and $ZnFe_2O_4$@1000 nanoparticles are comparable. Thus, the little difference in the crystallites sizes of samples treated at 800 and 1000 °C means the rate or degree of annealing decreases with the increasing crystallite size [46].

Table 1. The structural properties of $ZnFe_2O_4$ nanoparticles, annealed at different temperatures (T).

Sample	T (°C)	D (nm)	a (Å)	V (Å^3)	d_{311} (Å)	ρ_{xrd} (g/cm^3)	S (m^2/g)
BM-$ZnFe_2O_4$	-	9.30	8.445	602.3	2.546	5.321	121.24
$ZnFe_2O_4$@600	600	18.71	8.430	599.0	2.542	5.350	59.94
$ZnFe_2O_4$@800	800	23.03	8.424	597.8	2.540	5.361	48.59
$ZnFe_2O_4$@1000	1000	23.25	8.420	597.0	2.539	5.368	48.07

On the other hand, the lattice parameter decreases with the increase in annealing temperature, as shown in Figure 3e. Although this is contrary to the findings reported earlier that demonstrate an increase in the lattice parameter upon high-temperature annealing [47–49], the lattice parameter and crystal structure essentially depend on the processing method and conditions. As discussed above, in the starting sample, as-synthesized BM-$ZnFe_2O_4$ nanoparticles exhibit a random spinel structure with a certain degree of inversion that is inherently observed for the ball-milled $ZnFe_2O_4$ nanoparticles [32,33]. The reduction in the lattice parameter of annealed $ZnFe_2O_4$ nanoparticles can be explained by the redistribution of cations and crystal defects (oxygen vacancies).

During the high-temperature annealing process, both Zn^{2+} and Fe^{3+} cations may alter positions that influence the crystal structure. For instance, Lemine et al. [50] demonstrated that a decrease in the lattice parameter (from 8.448 to 8.427 Å) was caused by the redistribution of cations within the interstitial sites. However, this can also be attributed to the crystal defects [39,51]. It is a well-known fact that high-temperature annealing induces lattice defects and distortions. Furthermore, in the case

of nanocrystalline $ZnFe_2O_4$, it is believed that Zn^{2+} ions due to their volatile nature escape from the lattice during thermal treatment that successively results in oxygen vacancies [39,52]. Thus, a decrease in the lattice parameter (from 8.445 Å for BM-$ZnFe_2O_4$ to 8.420 Å for $ZnFe_2O_4$@1000) is attributed to the cationic redistribution (distortion) and lattice compression caused by escaping Zn^{2+} ions and oxygen vacancies.

Consequently, the interplanar distance and the volume of the annealed $ZnFe_2O_4$ nanoparticles are reduced as a function of the annealing temperature. On the other hand, the X-ray density increases (from 5.321 g cm^{-3} for BM-$ZnFe_2O_4$ to 5.368 g cm^{-3} for $ZnFe_2O_4$@1000) with the increase in annealing temperature. However, as shown in Table 1, the specific surface area is reduced to 48 m^2 g^{-1} due to an increase in the crystallite size of the annealed $ZnFe_2O_4$ nanoparticles. These results demonstrate that $ZnFe_2O_4$@1000 and $ZnFe_2O_4$@800 nanoparticles have bigger crystallite size and smaller specific surface area, but the greatest number of defect sites (as oxygen vacancies) and a geometrically frustrated [53] or distorted cubic spinel crystal structure compared to as-synthesized BM-$ZnFe_2O_4$ nanoparticles.

Figure 4a–c shows the SEM images of $ZnFe_2O_4$ nanoparticles annealed at different temperatures. An increase in the annealing temperature (to 1000 °C) results in a more compact surface, as shown in Figure 4c: the micrograph of $ZnFe_2O_4$@1000 nanoparticles. On the other hand, $ZnFe_2O_4$@600 nanoparticles annealed at 600 °C (Figure 4a) show less compact surface morphology with smaller particle size and relatively less aggregation of nanoparticles into clusters. The $ZnFe_2O_4$@800 nanoparticles demonstrate a similar surface morphology with slightly larger aggregates of nanoparticles, as shown in Figure 4b.

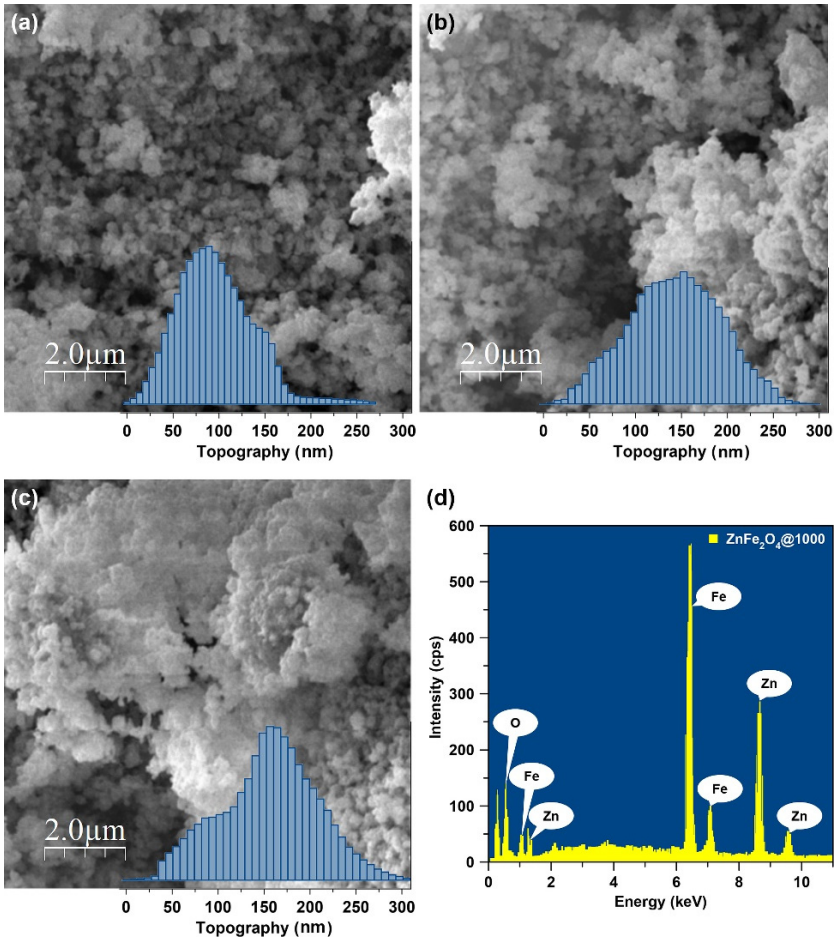

Figure 4. Scanning electron microscopy images of $ZnFe_2O_4$ nanoparticles annealed at (**a**) 600, (**b**) 800, and (**c**) 1000 °C. The respective histograms are given in the inset. (**d**) Energy-dispersive X-ray spectrum of $ZnFe_2O_4$ nanoparticles annealed at 1000 °C.

The image analysis of the scanning electron micrographs (via WSxM freeware [54]) shows the size distribution of $ZnFe_2O_4$ nanoparticles and the respective histograms are presented as insets in Figure 4a–c. $ZnFe_2O_4$@600 nanoparticles exhibit narrow size distribution with an average aggregate size of 100.2 nm, while $ZnFe_2O_4$@800 and $ZnFe_2O_4$@1000 nanoparticles reveal a relatively broad size distribution and an average aggregate size of 143.8 and 146.5 nm, respectively.

Figure 5 shows three-dimensional surface micrographs and topographic profiles of the sensing layers composed of $ZnFe_2O_4$ nanoparticles annealed at different temperatures. $ZnFe_2O_4$@600 surface exhibits a relatively smooth profile and roughness (Figure 5a). On the other hand, $ZnFe_2O_4$@800 (Figure 5b) and $ZnFe_2O_4$@1000 (Figure 5c) nanoparticles demonstrate higher roughness, greater particle size, and cluster formation. Thus, both X-ray diffraction and microscopic results indicate that $ZnFe_2O_4$ nanoparticles annealed at 800 and 1000 °C exhibit bigger crystallite size and a compact surface microstructure compared to those annealed at 600 °C.

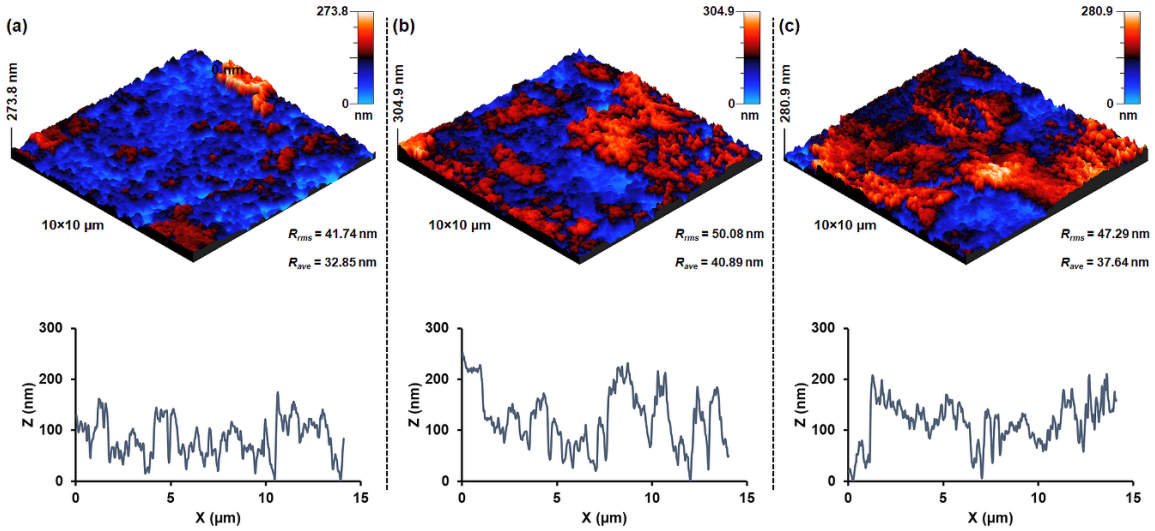

Figure 5. Three-dimensional micrographs and surface profiles showing the surface morphology, roughness, and topography of the sensitive element–$ZnFe_2O_4$ nanoparticles annealed at (**a**) 600, (**b**) 800, and (**c**) 1000 °C.

Table 2 presents the elemental composition of the annealed $ZnFe_2O_4$ nanoparticles. Compared to theoretically calculated values (wt.% or at.%), annealed $ZnFe_2O_4$ nanoparticles exhibit variations. As the annealing temperature increases, the relative percentage of Fe increases while the proportions of Zn and O decrease. A decrease in the oxygen content with increasing temperature is attributed to the oxygen vacancies and lattice defects. In addition, the atomic ratio of Fe/Zn is found to be 2.07, 2.20, and 2.21 for $ZnFe_2O_4$@600, $ZnFe_2O_4$@800, and $ZnFe_2O_4$@1000 nanoparticles, respectively. The increase in the Fe/Zn ratio as a function of annealing temperature may be attributed to the volatile nature of Zn^{2+} ions [39], as discussed earlier. Thus, the results are consistent and exhibit the microstructure evolution in the annealed $ZnFe_2O_4$ nanoparticles as a function of annealing temperature.

Table 2. The chemical composition of $ZnFe_2O_4$ nanoparticles annealed at different temperatures.

Sample	Zn		Fe		O	
	(wt.%)	(at.%)	(wt.%)	(at.%)	(wt.%)	(at.%)
$ZnFe_2O_4$@600	26.61	14.08	47.15	29.17	26.24	56.75
$ZnFe_2O_4$@800	25.60	13.51	48.04	29.64	26.36	56.85
$ZnFe_2O_4$@1000	25.65	13.68	48.67	30.34	25.69	55.98

Figure 6 demonstrates the NO_2 gas response of $ZnFe_2O_4$ nanoparticles annealed at different temperatures. The sensor measurements are performed at 600 °C. The as-synthesized BM-$ZnFe_2O_4$ nanoparticles based chemiresistive devices are not stable at 600 °C and do not show a measurable response to NO_2 gas. On the other hand, all the annealed $ZnFe_2O_4$ samples show a significant measurable response to 100–400 ppm NO_2, as shown in Figure 6. The sensor responses are generally saturated after ~4 min of exposure to the different concentrations of NO_2 gas. $ZnFe_2O_4$@1000 nanoparticles exhibit the highest NO_2 gas response, which is attributed to their greater stability at elevated temperatures and the presence of a large number of lattice defects. $ZnFe_2O_4$@600 and $ZnFe_2O_4$@800 nanoparticles also exhibit significant gas response at 600 °C. Peng et al. [55] recently demonstrated that the gas sensing properties of $ZnFe_2O_4$ nanoparticles could be enhanced by controlling the oxygen vacancies and that $ZnFe_2O_4$ nanoparticles with more oxygen vacancies revealed superior gas (acetone vapors) sensing performance at 280 °C. Thus, the higher NO_2 response of $ZnFe_2O_4$@1000 nanoparticles may be attributed to the oxygen vacancies resulting from high-temperature annealing of nanoparticles.

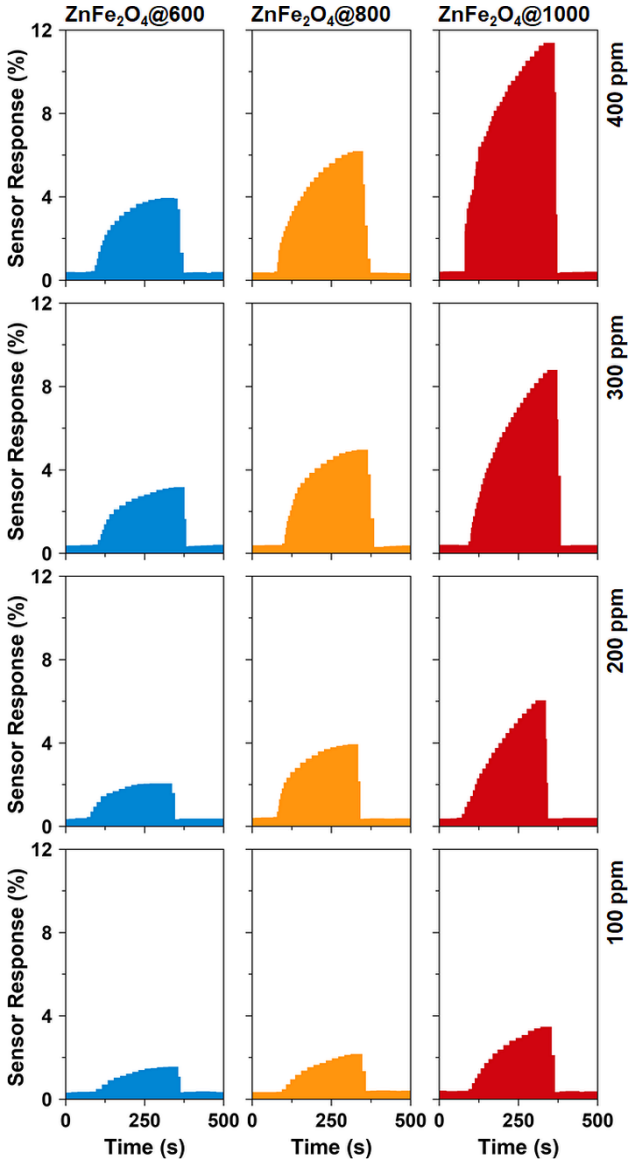

Figure 6. Time-dependent sensor response of the annealed $ZnFe_2O_4$ nanoparticles toward 100–400 ppm NO_2 gas at 600 °C.

Figure 7 shows the calibration curves obtained by plotting the maximum gas response of the annealed $ZnFe_2O_4$ nanoparticles as a function of gas concentration. All $ZnFe_2O_4$ samples exhibit a linear response in the concentration range of 100–400 ppm as demonstrated by the straight lines in Figure 7. The sensitivity of $ZnFe_2O_4$-based chemiresistive devices can be calculated from the slope of a straight line. The sensitivity of NO_2 sensors follows the order: $ZnFe_2O_4$@1000 > $ZnFe_2O_4$@800 > $ZnFe_2O_4$@600, which describes the effect of annealing temperature on sensor performance. An increase in annealing temperature improves the NO_2 sensing properties of $ZnFe_2O_4$ nanoparticles. Therefore, $ZnFe_2O_4$@1000 nanoparticles exhibit 2.0-fold and 3.2-fold high sensitivity compared to $ZnFe_2O_4$@800 and $ZnFe_2O_4$@600 nanoparticles, respectively.

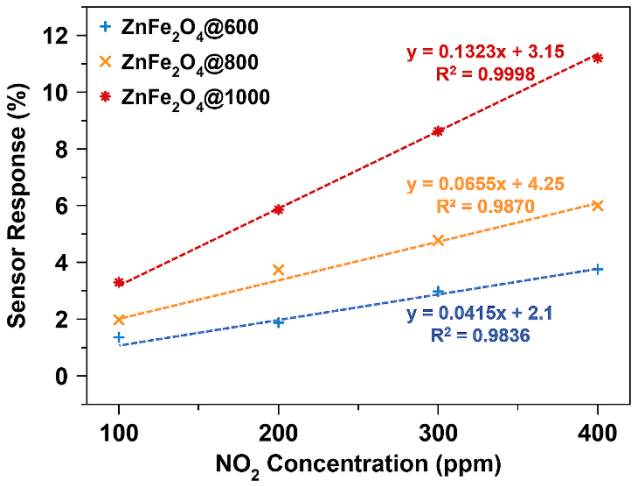

Figure 7. The calibration curves for different $ZnFe_2O_4$ samples showing NO_2 sensitivity of the chemiresistive devices.

Figure 8 shows the kinetics of $ZnFe_2O_4$-based chemiresistive gas sensors. The response (τ_{res}) and recovery (τ_{rec}) times of the annealed $ZnFe_2O_4$ nanoparticles are estimated from their response to 300 ppm NO_2 gas. All samples show fast response and recovery times. The response times are in the range of 145–195 s and follow the order: $ZnFe_2O_4$@800 > $ZnFe_2O_4$@600 > $ZnFe_2O_4$@1000. Thus, $ZnFe_2O_4$@1000 nanoparticles exhibit slightly longer response (τ_{res}) times compared to $ZnFe_2O_4$@600 and $ZnFe_2O_4$@800 nanoparticles. The recovery times are sharp (i.e., ≤20 s) for all samples and all sensors exhibit 100% recovery to their original state. At elevated temperatures, the recovery times are generally faster [10]. Overall, $ZnFe_2O_4$@1000 nanoparticles exhibit excellent NO_2 gas sensing properties such as high sensitivity, good response kinetics, and linear response in the tested concentration range.

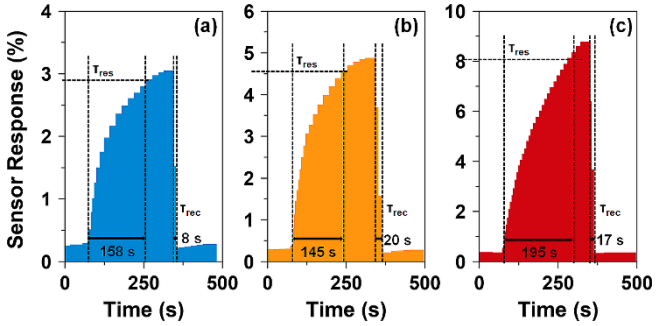

Figure 8. The response and recovery times of $ZnFe_2O_4$ nanoparticles annealed at (**a**) 600, (**b**) 800, and (**c**) 1000 °C calculated from their respective responses to 300 ppm NO_2.

The chemiresistive gas sensors function on the principles of changes in resistance of the sensing element when test gas molecules interact with the semiconductor surface [9]. Figure 9 demonstrates

the gas sensing mechanism of $ZnFe_2O_4$ nanoparticles. $ZnFe_2O_4$ is an *n*-type semiconductor [56]. In principle, when the $ZnFe_2O_4$-based chemiresistive device is exposed to air at elevated temperatures, active oxygen species are adsorbed on the surface of $ZnFe_2O_4$ nanoparticles. As shown in Figure 9a, O_2 molecules are physisorbed (O_2^-) at low temperatures (<200 °C) and subsequently chemisorbed (O^- and O^{2-}) at elevated temperatures (>200 °C) by capturing mobile electrons (e^-) from the surface. This leads to the formation of a charge depletion layer on the surface of $ZnFe_2O_4$ nanoparticles. Afterward, the surface is exposed to different concentrations of NO_2 gas and NO_2 being an electron-withdrawing molecule [57] further extracts mobile e^- from the surface or interacts with the chemisorbed oxygen species, as shown in Figure 9b. Consequently, the density of major charge carriers (e^-) decreases, and the thickness of the depletion region increases, which increases the resistance of the device. The redox reactions taking place on the surface of $ZnFe_2O_4$ nanoparticles are depicted in Figure 9.

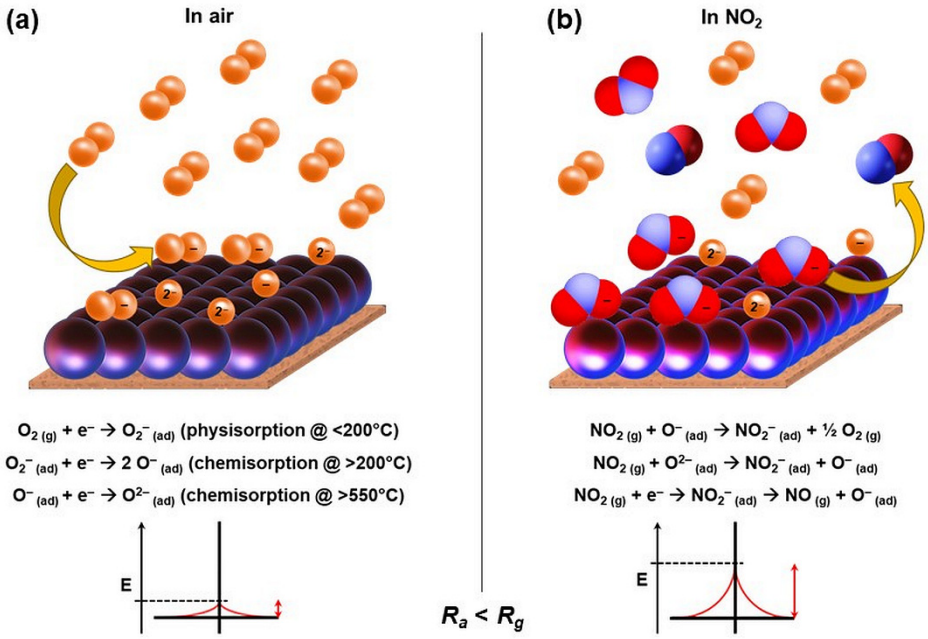

Figure 9. The gas sensing mechanism of $ZnFe_2O_4$ nanoparticles-based chemiresistive gas sensors.

Considering the mechanism described above, it is important to understand the behavior of $ZnFe_2O_4$ nanoparticles annealed at different temperatures. It is believed that semiconducting metal oxides with more oxygen vacancies adsorb a large number of active oxygen species, which in turn facilitates the surface redox reactions with the target gas molecules and improves the gas response [55]. Thus, oxygen vacancies and lattice defects play a major role in determining the gas response of $ZnFe_2O_4$ nanoparticles. Therefore, $ZnFe_2O_4$@1000 nanoparticles exhibit the best NO_2 gas sensing properties despite their slightly bigger crystallite size and smaller specific surface area. Table 3 shows a comparison of ferrite-based chemiresistive NO_2 sensors. The results demonstrate the potential of stable $ZnFe_2O_4$@1000 nanoparticles for high-temperature gas sensing applications.

Table 3. A comparison of the sensing properties of chemiresistive-type NO_2 gas sensors.

Material	Fabrication Method	Temperature (°C)	Detection Range (ppm)	Response † (S)	Response Time (s)	Recovery Time (s)	Reference
$CuFe_2O_4$	Coprecipitation	27	20–240	72%	8	5	[58]
$ZnFe_2O_4$	Hydrothermal	125	1–10	248 ‡	6.5	11	[59]
Pd-doped $BiFeO_3$	Sol-gel	140	50–3500	93%	60	100	[60]
$CoFe_2O_4$	Spray pyrolysis	150	20–80	95%	5	114	[61]
$ZnO/ZnFe_2O_4$	Wet chemical	200	0.1–20	~ 300 ‡	7	15	[25]
Cu-doped α-Fe_2O_3	Electrospinning	300	5–50	2 ‡	118	258	[62]
$ZnFe_2O_4$	Ball-milling	600	100–400	11%	195	17	This work
Sb-doped Zn_2SnO_4	Sputtering	600	50–300	~ 4 ‡	-	-	[63]

† The response (S) is reported for the highest tested concentration of NO_2 gas: $S(\%) = (R_g - R_a) \times 100/R_a$. ‡ If not reported as S(%), the response is measured as: $S = R_g/R_a$.

4. Conclusions

In summary, this study presents the effects of annealing temperature on the microstructure evolution and gas sensing properties of $ZnFe_2O_4$ nanoparticles. A high-energy ball-milling procedure is used to prepare pure $ZnFe_2O_4$ nanoparticles that are annealed at different temperatures (600–1000 °C). $ZnFe_2O_4$ nanoparticles exhibit a random spinel lattice structure that is distorted during high-temperature annealing. The XRD results show an increase in the crystallite size, but a reduction in the lattice parameter and volume that is attributed to the presence of lattice defects as oxygen vacancies. The oxygen vacancies play a major role in controlling the sensitivity of $ZnFe_2O_4$ nanoparticles. Thus, $ZnFe_2O_4$@1000 nanoparticles (annealed at 1000 °C) reveal the superior gas sensing properties with the highest sensitivity, good response kinetics, and linear response toward 100–400 ppm NO_2 gas. This is the first example of a $ZnFe_2O_4$@1000-based chemiresistive device showing significant gas response and stable sensor performance at 600 °C.

Author Contributions: Conceptualization, A.A.; methodology, A.A. and A.M.; validation, A.M. and N.I.; formal analysis, A.M., N.I. and R.J.; investigation, A.M. and N.I.; data curation, N.I., R.J. and U.Y.Q.; writing—original draft preparation, A.A.; writing—review and editing, A.A., A.M. and N.I.; visualization, A.M., R.J. and U.Y.Q.; project administration, A.A.; funding acquisition, A.A. All authors have read and agreed to the published version of the manuscript.

Funding: This research and the APC were funded by the Deanship of Scientific Research, University of Hafr Al Batin [grant number. G-107-2020].

Acknowledgments: The authors extend their appreciation to the Deanship of Scientific Research, University of Hafr Al Batin for funding this work through the research group project number G-107-2020.

Conflicts of Interest: The authors declare no conflict of interest. The funders had no role in the design of the study; in the collection, analyses, or interpretation of data; in the writing of the manuscript, or in the decision to publish the results.

References

1. Sun, Y.; Zwolińska, E.; Chmielewski, A.G. Abatement technologies for high concentrations of NO_x and SO_2 removal from exhaust gases: A review. *Crit. Rev. Environ. Sci. Technol.* **2016**, *46*, 119–142. [CrossRef]
2. Air Quality Standards: 2008/50/EC Directive on Ambient Air Quality and Cleaner Air for Europe. Available online: https://www.eea.europa.eu/themes/air/air-quality-concentrations/air-quality-standards (accessed on 28 April 2020).
3. Casquero-Vera, J.A.; Lyamani, H.; Titos, G.; Borrás, E.; Olmo, F.J.; Alados-Arboledas, L. Impact of primary NO_2 emissions at different urban sites exceeding the European NO_2 standard limit. *Sci. Total Environ.* **2019**, *646*, 1117–1125. [CrossRef] [PubMed]
4. Kaplan, G.; Avdan, Z.Y.; Avdan, U. Spaceborne Nitrogen Dioxide Observations from the Sentinel-5P TROPOMI over Turkey. *Proceedings* **2019**, *18*, 4. [CrossRef]

5. Afzal, A.; Andersson, M.; Di Franco, C.; Ditaranto, N.; Cioffi, N.; Scamarcio, G.; Lloyd Spetz, A.; Torsi, L. Electrochemical deposition of gold on indium zirconate ($InZrO_x$ with In/Zr atomic ratio 1.0) for high temperature automobile exhaust gas sensors. *J. Solid State Electrochem.* **2015**, *19*, 2859–2868. [CrossRef]
6. Liu, F.; Wang, B.; Yang, X.; Guan, Y.; Sun, R.; Wang, Q.; Liang, X.; Sun, P.; Lu, G. High-temperature stabilized zirconia-based sensors utilizing MNb_2O_6 (M: Co, Ni and Zn) sensing electrodes for detection of NO_2. *Sens. Actuators B Chem.* **2016**, *232*, 523–530. [CrossRef]
7. Liu, F.; Wang, B.; Yang, X.; Guan, Y.; Wang, Q.; Liang, X.; Sun, P.; Wang, Y.; Lu, G. High-temperature NO_2 gas sensor based on stabilized zirconia and $CoTa_2O_6$ sensing electrode. *Sens. Actuators B Chem.* **2017**, *240*, 148–157. [CrossRef]
8. Dai, L.; Shi, M.; Han, W.; Meng, W.; He, Z.; Zhu, L.; Wang, L. High-temperature NO_2 sensor based on aluminum/indium co-doped lanthanum silicate oxyapatite electrolyte and cobalt-free perovskite oxide sensing electrode. *Sens. Actuators B Chem.* **2017**, *250*, 629–640. [CrossRef]
9. Ghosh, A.; Zhang, C.; Shi, S.Q.; Zhang, H. High-Temperature Gas Sensors for Harsh Environment Applications: A Review. *CLEAN Soil Air Water* **2019**, *47*, 1800491. [CrossRef]
10. Afzal, A.; Cioffi, N.; Sabbatini, L.; Torsi, L. NO_x sensors based on semiconducting metal oxide nanostructures: Progress and perspectives. *Sens. Actuators B Chem.* **2012**, *171–172*, 25–42. [CrossRef]
11. Dey, A. Semiconductor metal oxide gas sensors: A review. *Mater. Sci. Eng. B* **2018**, *229*, 206–217. [CrossRef]
12. Barsan, N.; Schierbaum, K. *Gas Sensors Based on Conducting Metal Oxides: Basic Understanding, Technology and Applications*; Elsevier: Amsterdam, The Netherlands, 2018; ISBN 978-0-12-811225-0.
13. Afzal, A. β-Ga_2O_3 nanowires and thin films for metal oxide semiconductor gas sensors: Sensing mechanisms and performance enhancement strategies. *J. Mater.* **2019**, *5*, 542–557. [CrossRef]
14. Miura, N.; Zhuiykov, S.; Ono, T.; Hasei, M.; Yamazoe, N. Mixed potential type sensor using stabilized zirconia and $ZnFe_2O_4$ sensing electrode for NOx detection at high temperature. *Sens. Actuators B Chem.* **2002**, *83*, 222–229. [CrossRef]
15. Wetchakun, K.; Samerjai, T.; Tamaekong, N.; Liewhiran, C.; Siriwong, C.; Kruefu, V.; Wisitsoraat, A.; Tuantranont, A.; Phanichphant, S. Semiconducting metal oxides as sensors for environmentally hazardous gases. *Sens. Actuators B Chem.* **2011**, *160*, 580–591. [CrossRef]
16. Joshi, N.; Hayasaka, T.; Liu, Y.; Liu, H.; Oliveira, O.N.; Lin, L. A review on chemiresistive room temperature gas sensors based on metal oxide nanostructures, graphene and 2D transition metal dichalcogenides. *Microchim. Acta* **2018**, *185*, 213. [CrossRef] [PubMed]
17. Li, L.; Tan, J.; Dun, M.; Huang, X. Porous $ZnFe_2O_4$ nanorods with net-worked nanostructure for highly sensor response and fast response acetone gas sensor. *Sens. Actuators B Chem.* **2017**, *248*, 85–91. [CrossRef]
18. Lv, L.; Wang, Y.; Cheng, P.; Zhang, B.; Dang, F.; Xu, L. Ultrasonic spray pyrolysis synthesis of three-dimensional $ZnFe_2O_4$-based macroporous spheres for excellent sensitive acetone gas sensor. *Sens. Actuators B Chem.* **2019**, *297*, 126755. [CrossRef]
19. Khurshid, R.; Ali, F.; Afzal, A.; Ali, Z.; Qureshi, M.T. Polyol-mediated coprecipitation and aminosilane grafting of superparamagnetic, spinel $ZnFe_2O_4$ nanoparticles for room-temperature ethanol sensors. *J. Electrochem. Soc.* **2019**, *166*, B258–B265. [CrossRef]
20. Nemufulwi, M.I.; Swart, H.C.; Mdlalose, W.B.; Mhlongo, G.H. Size-tunable ferromagnetic $ZnFe_2O_4$ nanoparticles and their ethanol detection capabilities. *Appl. Surf. Sci.* **2020**, *508*, 144863. [CrossRef]
21. Dong, C.; Liu, X.; Xiao, X.; Du, S.; Wang, Y. Monodisperse $ZnFe_2O_4$ nanospheres synthesized by a nonaqueous route for a highly slective low-ppm-level toluene gas sensor. *Sens. Actuators B Chem.* **2017**, *239*, 1231–1236. [CrossRef]
22. Gao, X.; Sun, Y.; Zhu, C.; Li, C.; Ouyang, Q.; Chen, Y. Highly sensitive and selective H_2S sensor based on porous $ZnFe_2O_4$ nanosheets. *Sens. Actuators B Chem.* **2017**, *246*, 662–672. [CrossRef]
23. Zhang, H.-J.; Meng, F.-N.; Liu, L.-Z.; Chen, Y.-J.; Wang, P.-J. Highly sensitive H_2S sensor based on solvothermally prepared spinel $ZnFe_2O_4$ nanoparticles. *J. Alloys Compd.* **2018**, *764*, 147–154. [CrossRef]
24. Fareed, S.; Jamil, A.; Afsar, F.; Sher, F.; Li, C.; Xu, X.; Rafiq, M.A. Selective Oxygen Sensor Prepared Using Ni-doped Zinc Ferrite Nanoparticles. *J. Electron. Mater.* **2019**, *48*, 5677–5685. [CrossRef]
25. Runa, A.; Zhang, X.; Wen, G.; Zhang, B.; Fu, W.; Yang, H. Actinomorphic flower-like n-ZnO/p-$ZnFe_2O_4$ composite and its improved NO_2 gas-sensing property. *Mater. Lett.* **2018**, *225*, 73–76. [CrossRef]
26. Holzwarth, U.; Gibson, N. The Scherrer equation versus the "Debye-Scherrer equation". *Nat. Nanotechnol.* **2011**, *6*, 534. [CrossRef]

27. Satalkar, M.; Kane, S.N. On the study of Structural properties and Cation distribution of Zn $_{0.75-x}$ Ni $_{x}$ Mg $_{0.15}$ Cu $_{0.1}$ Fe $_{2}$ O $_{4}$ nano ferrite: Effect of Ni addition. *J. Phys. Conf. Ser.* **2016**, *755*, 012050. [CrossRef]
28. Afzal, A.; Abuilaiwi, F.A.; Javaid, R.; Ali, F.; Habib, A. Solid-state synthesis of heterogeneous $Ni_{0.5}Cu_{0.5-x}Zn_xFe_2O_4$ spinel oxides with controlled morphology and tunable dielectric properties. *J. Mater. Sci. Mater. Electron.* **2020**, *31*, 14261–14270. [CrossRef]
29. Gomes, J.A.; Azevedo, G.M.; Depeyrot, J.; Mestnik-Filho, J.; da Silva, G.J.; Tourinho, F.A.; Perzynski, R. $ZnFe_2O_4$ nanoparticles for ferrofluids: A combined XANES and XRD study. *J. Magn. Magn. Mater.* **2011**, *323*, 1203–1206. [CrossRef]
30. Manikandan, A.; Judith Vijaya, J.; Sundararajan, M.; Meganathan, C.; Kennedy, L.J.; Bououdina, M. Optical and magnetic properties of Mg-doped $ZnFe_2O_4$ nanoparticles prepared by rapid microwave combustion method. *Superlattices Microstruct.* **2013**, *64*, 118–131. [CrossRef]
31. Ferrari, S.; Kumar, R.S.; Grinblat, F.; Aphesteguy, J.C.; Saccone, F.D.; Errandonea, D. In-situ high-pressure x-ray diffraction study of zinc ferrite nanoparticles. *Solid State Sci.* **2016**, *56*, 68–72. [CrossRef]
32. Chinnasamy, C.N.; Narayanasamy, A.; Ponpandian, N.; Chattopadhyay, K. The influence of Fe^{3+} ions at tetrahedral sites on the magnetic properties of nanocrystalline $ZnFe_2O_4$. *Mater. Sci. Eng. A* **2001**, *304–306*, 983–987. [CrossRef]
33. Ehrhardt, H.; Campbell, S.J.; Hofmann, M. Structural evolution of ball-milled $ZnFe_2O_4$. *J. Alloys Compd.* **2002**, *339*, 255–260. [CrossRef]
34. Fella, O.O.; Tamine, M.; Randrianantoandro, N.; Grenèche, J.M. Microstructural Studies of Milled and Annealed $ZnFe_2O_4$ Nanostructures Using X-Ray Diffraction and Mössbauer Spectroscopy. *Nanosci. Nanoeng.* **2013**, *1*, 1–6.
35. Goldman, A. Crystal Structure of Ferrites. In *Handbook of Modern Ferromagnetic Materials*; Goldman, A., Ed.; The Springer International Series in Engineering and Computer Science; Springer US: Boston, MA, USA, 1999; pp. 207–227. ISBN 978-1-4615-4917-8.
36. Qin, M.; Shuai, Q.; Wu, G.; Zheng, B.; Wang, Z.; Wu, H. Zinc ferrite composite material with controllable morphology and its applications. *Mater. Sci. Eng. B* **2017**, *224*, 125–138. [CrossRef]
37. Fritsch, D. Electronic and optical properties of spinel zinc ferrite: Ab-initio hybrid functional calculations. *J. Phys. Condens. Matter* **2018**, *30*, 095502. [CrossRef]
38. Li, G.; Zhu, X.; Song, W.; Yang, Z.; Dai, J.; Sun, Y.; Fu, Y. Annealing Effects on Semitransparent and Ferromagnetic $ZnFe_2O_4$ Nanostructured Films by Sol–Gel. *J. Am. Ceram. Soc.* **2011**, *94*, 2872–2877. [CrossRef]
39. Yadav, R.S.; Kuřitka, I.; Vilcakova, J.; Urbánek, P.; Machovsky, M.; Masař, M.; Holek, M. Structural, magnetic, optical, dielectric, electrical and modulus spectroscopic characteristics of $ZnFe_2O_4$ spinel ferrite nanoparticles synthesized via honey-mediated sol-gel combustion method. *J. Phys. Chem. Solids* **2017**, *110*, 87–99. [CrossRef]
40. Solano, E.; Frontera, C.; Puig, T.; Obradors, X.; Ricart, S.; Ros, J. Neutron and X-ray diffraction study of ferrite nanocrystals obtained by microwave-assisted growth. A structural comparison with the thermal synthetic route. *J. Appl. Crystallogr.* **2014**, *47*, 414–420. [CrossRef]
41. Zhang, J.; Song, J.-M.; Niu, H.-L.; Mao, C.-J.; Zhang, S.-Y.; Shen, Y.-H. $ZnFe_2O_4$ nanoparticles: Synthesis, characterization, and enhanced gas sensing property for acetone. *Sens. Actuators B Chem.* **2015**, *221*, 55–62. [CrossRef]
42. Xu, X.; Xiao, L.; Haugen, N.O.; Wu, Z.; Jia, Y.; Zhong, W.; Zou, J. High humidity response property of sol–gel synthesized $ZnFe_2O_4$ films. *Mater. Lett.* **2018**, *213*, 266–268. [CrossRef]
43. Sintering and Grain Growth. In *Ceramic Materials: Science and Engineering*; Carter, C.B.; Norton, M.G., Eds.; Springer: New York, NY, USA, 2007; pp. 427–443. ISBN 978-0-387-46271-4.
44. Ranjith Kumar, E.; Arunkumar, T.; Prakash, T. Heat treatment effects on structural and dielectric properties of Mn substituted $CuFe_2O_4$ and $ZnFe_2O_4$ nanoparticles. *Superlattices Microstruct.* **2015**, *85*, 530–535. [CrossRef]
45. Van Hoang, N.; Hung, C.M.; Hoa, N.D.; Van Duy, N.; Van Hieu, N. Facile on-chip electrospinning of $ZnFe_2O_4$ nanofiber sensors with excellent sensing performance to H2S down ppb level. *J. Hazard. Mater.* **2018**, *360*, 6–16. [CrossRef] [PubMed]
46. Wilder, D.R.; Fitzsimmons, E.S. Further Study of Sintering Phenomena. *J. Am. Ceram. Soc.* **1955**, *38*, 66–71. [CrossRef]

47. Yadav, R.S.; Havlica, J.; Masilko, J.; Tkacz, J.; Kuřitka, I.; Vilcakova, J. Anneal-tuned structural, dielectric and electrical properties of $ZnFe_2O_4$ nanoparticles synthesized by starch-assisted sol–gel auto-combustion method. *J. Mater. Sci. Mater. Electron.* **2016**, *27*, 5992–6002. [CrossRef]
48. Kombaiah, K.; Vijaya, J.J.; Kennedy, L.J.; Bououdina, M. Studies on the microwave assisted and conventional combustion synthesis of Hibiscus rosa-sinensis plant extract based $ZnFe_2O_4$ nanoparticles and their optical and magnetic properties. *Ceram. Int.* **2016**, *42*, 2741–2749. [CrossRef]
49. Kombaiah, K.; Vijaya, J.J.; Kennedy, L.J.; Bououdina, M. Optical, magnetic and structural properties of $ZnFe_2O_4$ nanoparticles synthesized by conventional and microwave assisted combustion method: A comparative investigation. *Optik* **2017**, *129*, 57–68. [CrossRef]
50. Lemine, O.M.; Bououdina, M.; Sajieddine, M.; Al-Saie, A.M.; Shafi, M.; Khatab, A.; Al-Hilali, M.; Henini, M. Synthesis, structural, magnetic and optical properties of nanocrystalline $ZnFe_2O_4$. *Phys. B Condens. Matter* **2011**, *406*, 1989–1994. [CrossRef]
51. Nikolic, M.V.; Vasiljevic, Z.Z.; Lukovic, M.D.; Pavlovic, V.P.; Krstic, J.B.; Vujancevic, J.; Tadic, N.; Vlahovic, B.; Pavlovic, V.B. Investigation of $ZnFe_2O_4$ spinel ferrite nanocrystalline screen-printed thick films for application in humidity sensing. *Int. J. Appl. Ceram. Technol.* **2019**, *16*, 981–993. [CrossRef]
52. Sivakumar, N.; Narayanasamy, A.; Ponpandian, N.; Govindaraj, G. Grain size effect on the dielectric behavior of nanostructured $Ni_{0.5}Zn_{0.5}Fe_2O_4$. *J. Appl. Phys.* **2007**, *101*, 084116. [CrossRef]
53. Salcedo Rodríguez, K.L.; Stewart, S.J.; Mendoza Zélis, P.M.; Pasquevich, G.A.; Rodríguez Torres, C.E. Role of defects on the magnetic behaviour of the geometrically frustrated spinel $ZnFe_2O_4$. *J. Alloys Compd.* **2018**, *752*, 289–295. [CrossRef]
54. Horcas, I.; Fernández, R.; Gómez-Rodríguez, J.M.; Colchero, J.; Gómez-Herrero, J.; Baro, A.M. WSXM: A software for scanning probe microscopy and a tool for nanotechnology. *Rev. Sci. Instrum.* **2007**, *78*, 013705. [CrossRef]
55. Peng, S.; Wang, Z.; Liu, R.; Bi, J.; Wu, J. Controlled oxygen vacancies of $ZnFe_2O_4$ with superior gas sensing properties prepared via a facile one-step self-catalyzed treatment. *Sens. Actuators B Chem.* **2019**, *288*, 649–655. [CrossRef]
56. Jeseentharani, V.; George, M.; Jeyaraj, B.; Dayalan, A.; Nagaraja, K.S. Synthesis of metal ferrite (MFe_2O_4, M = Co, Cu, Mg, Ni, Zn) nanoparticles as humidity sensor materials. *J. Exp. Nanosci.* **2013**, *8*, 358–370. [CrossRef]
57. Valero, E.L. *Advanced Nanomaterials for Inexpensive Gas Microsensors: Synthesis, Integration and Applications*; Elsevier: Amsterdam, The Netherlands, 2019; ISBN 978-0-12-814828-0.
58. Rathore, D.; Mitra, S.; Kurchania, R.; Pandey, R.K. Physicochemical properties of $CuFe_2O_4$ nanoparticles as a gas sensor. *J. Mater. Sci. Mater. Electron.* **2018**, *29*, 1925–1932. [CrossRef]
59. Li, K.; Luo, Y.; Liu, B.; Gao, L.; Duan, G. High-performance NO_2-gas sensing of ultrasmall $ZnFe_2O_4$ nanoparticles based on surface charge transfer. *J. Mater. Chem. A* **2019**, *7*, 5539–5551. [CrossRef]
60. Waghmare, S.D.; Raut, S.D.; Ghule, B.G.; Jadhav, V.V.; Shaikh, S.F.; Al-Enizi, A.M.; Ubaidullah, M.; Nafady, A.; Thamer, B.M.; Mane, R.S. Pristine and palladium-doped perovskite bismuth ferrites and their nitrogen dioxide gas sensor studies. *J. King Saud Univ. Sci.* **2020**, *32*, 3125–3130. [CrossRef]
61. Bagade, A.A.; Rajpure, K.Y. Development of $CoFe_2O_4$ thin films for nitrogen dioxide sensing at moderate operating temperature. *J. Alloys Compd.* **2016**, *657*, 414–421. [CrossRef]
62. Wu, R.-A.; Wei Lin, C.; Tseng, W.J. Preparation of electrospun Cu-doped α-Fe_2O_3 semiconductor nanofibers for NO_2 gas sensor. *Ceram. Int.* **2017**, *43*, S535–S540. [CrossRef]
63. Yamada, Y.; Seno, Y.; Masuoka, Y.; Yamashita, K. Nitrogen oxides sensing characteristics of Zn_2SnO_4 thin film. *Sens. Actuators B Chem.* **1998**, *49*, 248–252. [CrossRef]